

#### Contents lists available at ScienceDirect

### Petroleum Science

journal homepage: www.keaipublishing.com/en/journals/petroleum-science



### Original Paper

### The new multistage water adsorption model of Longmaxi Formation shale considering the spatial configuration relationship between organic matter and clay minerals



Zhi-Ye Gao <sup>a, b</sup>, Shu-Ling Xiong <sup>a, b, \*</sup>, Lin Wei <sup>c, \*\*</sup>

- <sup>a</sup> State Key Laboratory of Petroleum Resources and Prospecting, China University of Petroleum, Beijing, 102249, China
- <sup>b</sup> Unconventional Petroleum Research Institute, China University of Petroleum, Beijing, 102249, China
- <sup>c</sup> School of Energy Resources, China University of Geosciences, Beijing, 100083, China

#### ARTICLE INFO

#### Article history: Received 17 November 2021 Received in revised form 9 February 2022 Accepted 26 May 2022 Available online 31 May 2022

Edited by Teng Zhu

Keywords: Longmaxi formation shale Water content OM-clay complexes Spatial occurrence relationship

#### ABSTRACT

The water adsorption by shale significantly affects shale gas content and its seepage capacity. However, the mechanism of water adsorption by shale is still unclear due to its strong heterogeneity and complicated pore structure. The relationship between the adsorbed water content at different relative humidities (RHs) and shale compositions, as well as shale pore structure and the spatial configuration relationship between organic matter (OM) and clay minerals, was investigated to clarify the controlling factors and mechanisms of water adsorption by Longmaxi Formation shale from the Southern Sichuan Basin in China. Consequently, the water adsorption process could be generally divided into three different stages from 0%RH to 99%RH. Furthermore, the Johnston's clay mineral interlayer pore structure model (JCM), the Freundlich model (FM) and the Dubinin-Astakhov model (DAM) were tested to fit the three water adsorption stages from low RH to high RH, respectively. The fitting results of the ICM and FM at lower RHs were far from good, while the fitting results of DAM at higher RHs were acceptable. Accordingly, two revised models (LRHM and MRHM) considering the spatial configuration relationship between OM and clay minerals were proposed for the two stages with lower RHs, and performed better fitting results indicating the pronounced effect of the spatial configuration relationship between OM and clay minerals on the water adsorption process of Longmaxi Formation shale. The outcomes of this study will contribute to clarifying the water distribution characteristics in the pore network of shale samples with variable water contents.

© 2022 The Authors. Publishing services by Elsevier B.V. on behalf of KeAi Communications Co. Ltd. This is an open access article under the CC BY-NC-ND license (http://creativecommons.org/licenses/by-nc-nd/4.0/).

#### 1. Introduction

Since the breakthrough of shale gas exploration in North America in 1998, the global energy pattern has changed gradually (Zou et al., 2017). Nowadays, shale gas resources account for about one half of the total unconventional natural gas resources (e.g. coal bed methane, tight sandstone gas and shale gas) (Li et al., 2009). China has plenty of shale gas resources, with recoverable shale gas resources of about  $26 \times 10^{12}$  m $^3$  (Zhang et al., 2009).

It has been reported that some specific gas-bearing shale

*E-mail addresses*: 2018210206@student.cup.edu (S.-L. Xiong), linwei@cugb.edu. cn (L. Wei).

formations contain water at reservoir conditions, and the initial water in shale could be classified as free water and irreducible water based on its mobility (Cheng et al., 2017). Previous studies have proven that clay minerals are the main occurrence position of water with strong hydrophilicity. More specifically, water molecules distribute in clay minerals in capillary water state and water film state (Feng et al., 2018). The initial water in shale reservoirs is mainly produced by two mechanisms, 1) During the depositional process and early diagenesis stage, pore spaces are mainly filled by inherited sedimentary water. With the increase of buried depth, the inherited sedimentary water within pore spaces is gradually expelled. However, some amount of inherited sedimentary water is retained in the shale pore spaces due to the protection of brittle minerals against compaction (Goulty et al., 2016; Cicchino et al., 2014); 2) With the diagenetic and thermal evolution of shale, the

<sup>\*</sup> Corresponding author.

<sup>\*\*</sup> Corresponding author.

conversion of clay minerals (such as montmorillonite losing interlayer water and changing to illite) and the pyrolysis of kerogen can generate water (Ola et al., 2018).

The initial water content of Longmaxi Formation shale in the Sichuan Basin can be divided into two categories. The first category is shale reservoir of ultra-high water content, almost higher than 60%, which is located in the tectonic reconstruction areas at the edge of the basin. Intense tectonic activities caused the natural gas to escape and the water permeated into the reservoir. The second category is shale reservoir of low water content, part of which is lower than 45%, located in tectonic stable regions within the basin (Fang et al., 2014). Cheng et al. (2018) reported that the water content in inorganic-hosted pores ( $S_{iw}$ ) of Longmaxi Formation shale of Sichuan Basin is greater than the water content in organic-hosted pores ( $S_{ow}$ ), and the  $S_{iw}/S_{ow}$  ratio is 2.04.

Extensive studies have been conducted to investigate the water adsorption characteristics of shale and most studies believed that the water adsorption capacity of OM was weak (Mahajan and Walker, 1971; Nishino, 2001). Recently, researchers have gradually begun to pay more attention to the contribution of OM to the water adsorption process of shale (Gu et al., 2016; Cheng et al. 2017, 2018; Gao and Hu, 2018; Gao et al., 2020). However, the contribution of OM and clay minerals to shale water adsorption is mostly considered in wettability and pore structure (Merkel et al. 2015, 2016), while OM and clay mineral complexes were commonly observed in Longmaxi Formation shale (Ji et al., 2019; Zhu et al., 2020). The effect of different spatial configuration relationships between OM and clay minerals (such as clay mineral in OM or OM external clay mineral) on the water adsorption of shale is still unclear and to be clarified.

Shale with strong compositional heterogeneity in microscale is mainly composed of OM and inorganic minerals with different wettability, which complicates the water adsorption characteristics in shale. As to the wettability of OM, it changes from hydrophilicity at the immature stage to neutral wetting and eventually to hydrophobicity with the increase of thermal maturity due to the decreased H/C and O/C ratios during hydrocarbon generation process (Hu et al. 2015, 2016). However, clay minerals are generally hydrophilic, and different types of clay minerals have different water adsorption capacities in the order of montmorillonite > kaolinite > illite (Feng et al., 2018). With the increase of water content in shale, the occurrence form of water molecules in OM pores and clay mineral pores changes differently, showing different water adsorption mechanisms (Chen et al., 2021). For OM, water molecules are adsorbed by the oxygen-containing functional groups of OM when the water content is low. With the increase of water content, water molecules adsorbed on the surface of OM gradually gather to form water clusters (Hu et al. 2015, 2016). As to clay minerals, water molecules preferentially enter the interlayer pore spaces of clay minerals when the water content is low. With the increase of water content, the occurrence state of water molecules on the surface of clay minerals gradually changes from monolayer adsorption to a water film state, and finally to a capillary condensed state (Li et al., 2017; Feng et al., 2018). Yang et al. (2020a) reported that water molecules preferentially are adsorbed at the primary adsorption sites (mainly strong inorganic adsorption sites) in the low relative humidity (RH) region (i.e., <20% RH). With the RH increases, multilayer adsorption and capillary condensation of water molecules all occur in the intermediate RH region (i.e., 20–70% RH). And water clusters have gradually formed in certain parts of the hydrophobic pore spaces (mainly OM pores) in this stage. Finally, more and more water molecules occupied all the hydrophilic pores in the high RH region (i.e., >70-80% RH). However, Hou et al. (2021) indicated clay minerals initially facilitates the adsorption of water vapor at low RH stage (i.e., 2%), and OM

provides more sites for water in clusters at high RH stage (i.e., 95%). Consequently, existing researches of RH ranges for occurrence of water molecules in OM and inorganic pores of the Longmaxi Formation shale are disputable. Hence, the RH range (or water content range) for each occurrence form of water molecules in OM pores and clay mineral pores of Longmaxi Formation shale is still unknown and should be investigated.

Several adsorption models have been used to describe the adsorption process, including Langmuir model, Guggenheim-Anderson-de-Boer (GAB) model, Freundlich model, Dubinin-Astakhov model (Langmuir, 1917; Timmermann, 2003; Shen et al., 2018; Yang et al., 2020a). The Langmuir model provides a method to quantify the relationship between adsorbed gas and pressure (Langmuir, 1917). However, the Langmuir model has some limitations. Firstly, the Langmuir model is based on the adsorption of homogeneous surfaces while shale composed of complex organic and inorganic components is characterized by non-homogeneous surfaces (Feng et al., 2018). Secondly, the assumption of monolayer adsorption of Langmuir model is contradicted with the actual adsorption. Then, the revised model, Brunauer-Emmett-Teller (BET) model, was proposed based on multilayer adsorption (Li et al., 2015). Furthermore, the variations in the adsorption energies of monolayer or multilayer adsorption sites have been considered in the modified BET model (GAB model). Besides, the efficient RH range of GAB model covered RH from 5% to 95% (Timmermann, 2003). The Freundlich model is based on uneven surfaces, which is mainly used to describe the multilayer adsorption (Hatch et al., 2012). The Dubinin-Astakhov model is based on the micropore filling theory and can also describe the capillary condensation at high RHs (Feng et al., 2018). Overall, these adsorption models have its own pros and cons and could not perfectly describe the whole water adsorption process alone. Consequently, it is necessary to revise and integrate these models to clarify the water adsorption process in shale samples.

The presence of water in shale reservoir has a significant impact on the shale gas occurrence state and the total shale gas storage capacity, which affects the shale gas production behaviors and the decision process of exploitation strategy (Ge et al., 2015; Ghanbari and Dehghanpour, 2016; Wang et al., 2021). More specifically, the methane adsorption capacity of shale can be significantly reduced when the shale adsorbs water (Chalmers and Bustin, 2010; Jin and Firoozabadi, 2014; Merkel et al., 2016; Wang and Yu, 2016; Li et al., 2020). Consequently, it is of great practical significance to clarify the water adsorption characteristics of shale for guiding actual shale gas exploitation.

This work investigated the influence of pore structure, OM and inorganic minerals of shale on its water adsorption process. The Longmaxi Formation shale samples from the Southern Sichuan Basin were used in this study. Five different RH conditions (0%RH, 16%RH, 41%RH, 76%RH and 99%RH) were set and the water contents of shale samples under different RH conditions were calculated. The pore structure of shale samples was comprehensively analyzed by  $N_2$  adsorption, high-pressure mercury intursion porosimetry (HPMIP), and field-emission scanning electron microscopy (FE-SEM) with Image-Pro Plus (IPP) quantitative analysis software. Finally, the water adsorption characteristics of Longmaxi Formation shale and its controlling factors were clarified.

#### 2. Samples and experiments

Four Longmaxi Formation shale samples were selected from the four blocks of Changning, Luzhou, Yuxi and Weiyuan in the southern Sichuan Basin and the sampling location is shown in Fig. 1.

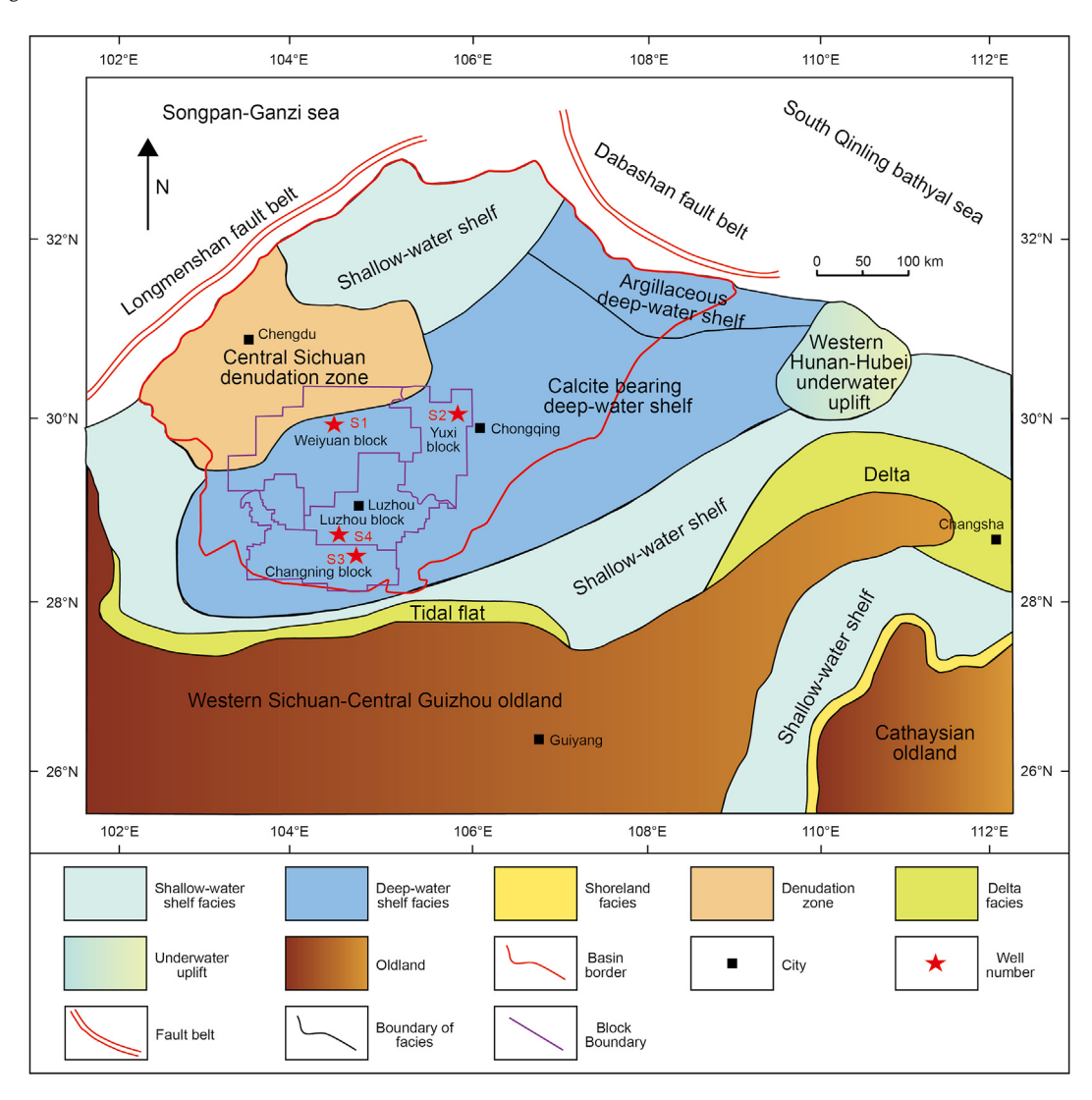


Fig. 1. The locations of Longmaxi Formation shale samples from the study area.

#### 2.1. TOC content and mineral composition analysis

Shale samples were ground to 40–60 mesh for TOC analysis and hydrochloric acid was used to remove the inorganic carbon. The TOC content was determined by using a LECO CS-230 analyzer.

Shale samples were ground to ~100 mesh for mineralogy analysis, which was accomplished by using the X-ray diffractometer (XRD) analysis (Ringaku MiniflexII). The XRD scanned shale samples from  $5^{\circ}$  to  $90^{\circ}$  with a scanning speed of  $2^{\circ}$ /min and a scanning step width of  $0.02^{\circ}$ .

#### 2.2. Pore structure characterization

The optimal pore size characterization range of  $N_2$  adsorption and HP-MIP tests is the mesopore (2–50 nm) and macropore (>50 nm), respectively (Jiang et al., 2016). Therefore, the  $N_2$  adsorption and HP-MIP experiments were combined to obtain the pore size distribution information of these shale samples. Before the  $N_2$  adsorption and HP-MIP experiments were conducted, shale samples were dried at 105 °C for at least 24 h to remove the water content within pore spaces. The  $N_2$  adsorption experiment was conducted on shale samples in 40–60 mesh by using a Quantachrome Autosorb IQ instrument. The specific surface area and pore

size distribution were obtained based on the BET theory and the Barrett–Joyner–Halenda (BJH) theory, respectively. The Micromeritics AutoPoreIV9500 was used to perform HP-MIP experiments on 1 cm<sup>3</sup> cubic shale samples. The pore size distribution was obtained according to Washburn equation (Washburn, 1921).

The pore structure of these shale samples was characterized directly by FE-SEM combined with argon-ion polishing technology. Two-dimensional images were analyzed by IPP (Image Pro Plus) software to obtain the quantitative pore structure parameters (e.g. pore size distribution, areal porosity and the areal fraction of one specific component).

#### 2.3. Water adsorption experiment

In order to remove the initial water in the pore spaces of shale samples, four core samples were ground into 20–40 mesh and dried for at least 24 h at 105 °C before the water adsorption experiment. In order to control the RH accurately and keep the experimental RH evenly distributed in the overall humidity range, five different RH conditions of known water vapor pressure were used in this study. Each shale sample was divided into five groups and each group went through one certain RH condition. For water adsorption experiment, shale samples were placed inside an

incubator with a container holding one of the four saturated salt solutions at a constant temperature of  $35\,^{\circ}\text{C}$  to establish a certain water vapor pressure: CH<sub>3</sub>COOK at 16%RH, K<sub>2</sub>CO<sub>3</sub> at 41%RH, NaCl at 76%RH and H<sub>2</sub>O at 99%RH. And all salts used in the experiment are with the purity of >99.0%. The equipment diagram was shown in Fig. 2. The determination method of water vapor pressure is referred to Greenspan (1977). The weight of the sample was measured at the 15th day, 32nd day, 47th day, 62nd day, 79th day, 124th day and 147th day.

#### 3. Results

#### 3.1. Compositional analysis

The TOC content and mineral composition of the four shale samples are shown in Fig. 3. These shale samples were dominated by siliceous minerals, carbonate minerals and clay minerals, accounting for 96.4 wt%~99.4 wt% of the total mineral composition. The siliceous mineral content of these shale samples was 13.8 wt% ~55.7 wt%, with an average value of 36.50 wt%. The carbonate mineral content of these shale samples was 5.2 wt%~63.4 wt%, and the average value was 25.98 wt%. The clay mineral content of these shale samples was 16.6 wt%~64.3 wt%, with an average value of 35.20 wt%. Illite was the main component of clay minerals in the Longmaxi Formation shale (Liu et al., 2016). The TOC content was 1.2 wt%~3.2 wt%, and the average value was 2.22 wt%. Moreover, the equivalent  $R_0$  of the Lower Silurian Longmaxi Formation shale in the Sichuan Basin was mainly distributed in the range of 2.0%~2.5%, indicating a stage of high-overhigh maturity (Wang et al., 2015).

#### 3.2. Pore structure characterization

#### 3.2.1. OM pore structure characteristics from FE-SEM

The FE-SEM images of OM pores of three shale samples— X2, X3, X4—are shown in Fig. 4. OM—clay complexes and OM pores existed in all the three shale samples. However, the shape, number

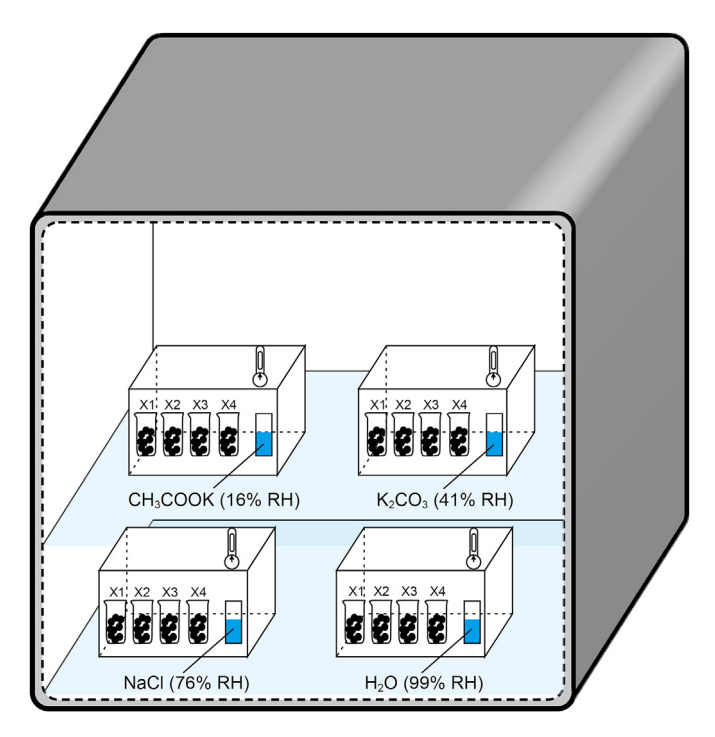


Fig. 2. The schematic of moisture-equilibrated water adsorption experiment. of moisture-equilibrated experiment.

and size of OM pores were greatly different. The OM in the OM—clay complexes developed more pores than isolated OM because clay minerals catalyzed the hydrocarbon generation process of OM (Liu et al., 2018).

FE-SEM technology and IPP image processing software were used to identify and calculate the number of OM pores with different pore diameters. As shown in Fig. 5, all the three shale samples developed many small OM pores but few large OM pores. Sample X2 developed the smallest OM pores and the fewest large OM pores, among which OM pores smaller than 9 nm accounted for 50.21% of the total, OM pores larger than 50 nm only accounted for 1.06% of the total, and OM pores larger than 100 nm were completely undeveloped. The proportions of OM pores smaller than 9 nm in X3 and X4 were 31.13% and 12.34%, respectively, and the proportions of OM pores greater than 50 nm were 7.57% and 10.44%, respectively.

# 3.2.2. The whole-aperture pore structure characteristics of shale samples by $N_2$ adsorption and HPMIP

As shown in Fig. 6, the specific surface area distribution of the four shale samples was characterized in the whole-aperture pore diameter range. There were several distribution peaks located in the pore diameter range of less than 10 nm, and the curve value tended to be 0 when the pore diameter was larger than 50 nm. This indicates that the mesopores contributed more to the specific surface area while the macropores contributed less. The pore volume distribution of shale samples is shown in Fig. 7. The pore volume of shale samples was mainly contributed by mesopores. The pore volumes of samples X1, X2 and X4 were mainly contributed by small-diameter mesopores (<30 nm), and the pore volume of pores less than 30 nm accounted for 77.14%, 81.01% and 82.96% of the total pore volume, respectively. The percentage of pore volumes of pores less than 9 nm in samples X1, X2 and X4 accounted for the largest proportion of total pore volume, accounting for 46.62%, 59.11% and 50.61%, respectively. The pore volume of sample X3 was contributed by larger pores, with pores less than 30 nm accounting for 45.49% and pores less than 9 nm only accounting for 18.80%.

#### 3.3. Water content

This study set up four RH levels (16% RH, 41% RH, 76% RH, 99% RH) and the results of water content in shale samples at different relative humidities (RHs) are shown in Fig. 8. When the RH was 16% RH, the water contents of samples X2, X3 and X4 basically reached an equilibrium state using 32 days, and the water content of sample X1 reached equilibrium using 15 days. When the RH was 41%RH, the water contents of samples X1, X2 and X3 basically reached an equilibrium state using 15 days while the sample X4 took 32 days. When the RH was 76%RH, the water contents of the four samples tended to be in equilibrium at the 47th day. When the RH was 99% RH, sample X1 did not finally reach the equilibrium state, while samples X2, X3 and X4 reached the equilibrium state at the 47th, 62nd and 79th day, respectively.

As shown in Fig. 9, the water adsorption curves had Type II IUPAC isotherms, which are typical for multilayer water adsorption of non-expansive clays such as illite. Sample X1 had the largest water adsorption capacity, which was about 2 times that of samples X3 and X4. The water adsorption capacity of sample X2 was in the middle of the range. When the RH was lower than 76%RH, the water content of the shale samples increased in a nearly linear manner with the increase of RH. When the RH was higher than 76%RH, the water content no longer increased linearly with the increase of RH. Samples X3 and X4 showed a similar water adsorption capacity in the full stage of RH and the water content of sample X4 was slightly higher than sample X3 when the RH was between 16%RH and 76%RH.

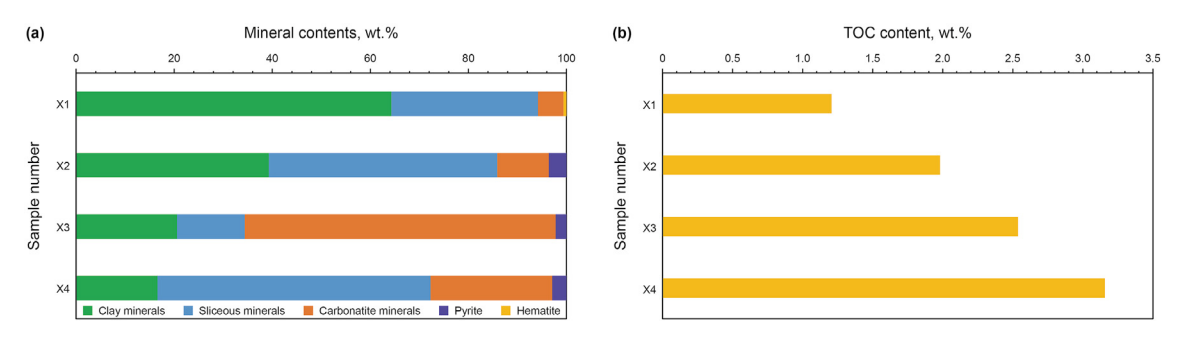


Fig. 3. OM content and mineral compositions of the sample.

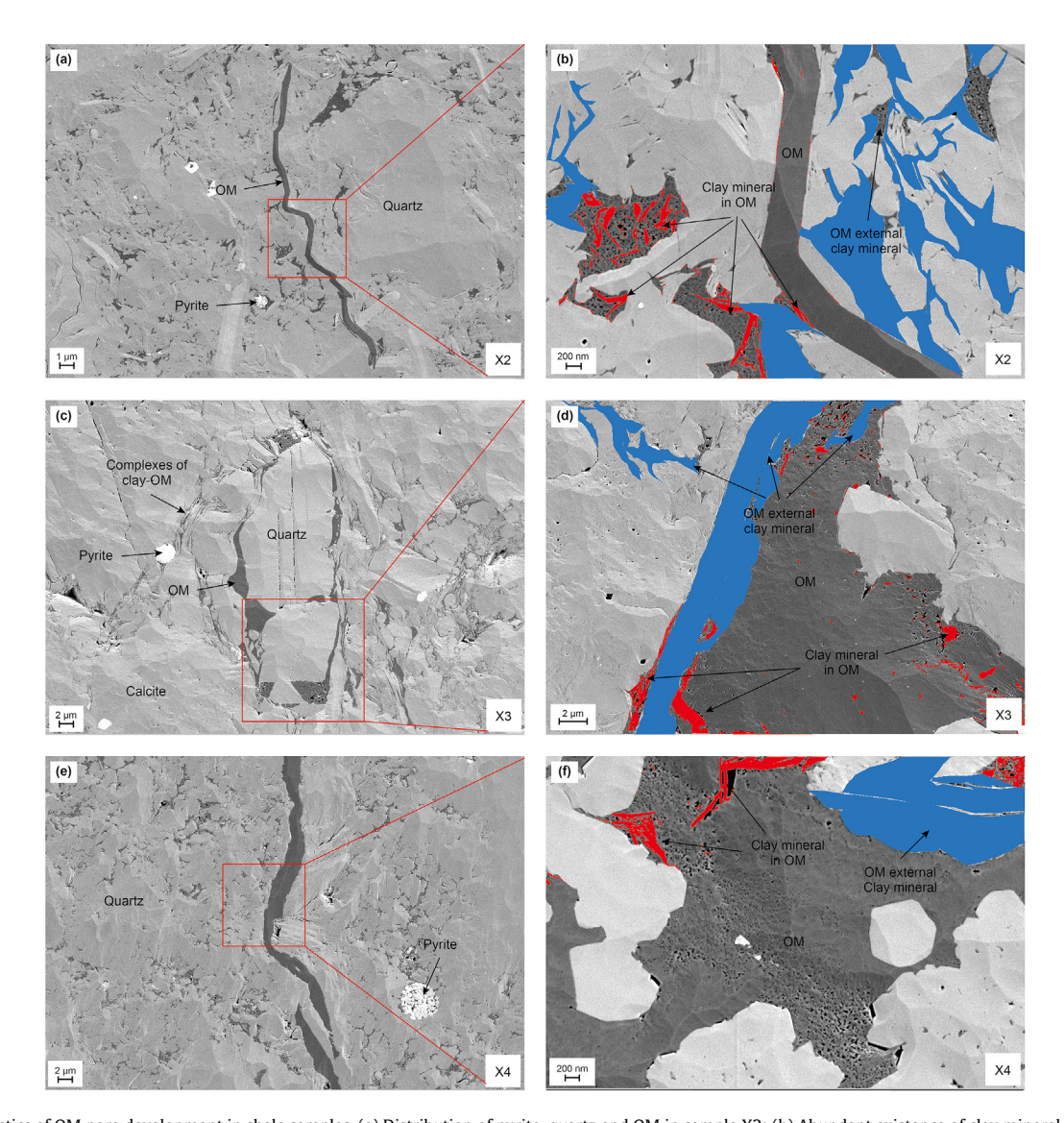


Fig. 4. Characteristics of OM pore development in shale samples. (a) Distribution of pyrite, quartz and OM in sample X2; (b) Abundant existence of clay mineral in OM (marked by red) and OM external clay mineral (marked by blue) in sample X2, the proportions of OM external clay in sample X2 is 96.9%; (c) Distribution of pyrite, quartz, calcite, complexes of clay-OM and OM in sample X3; (d) Abundant existence of clay mineral in OM (marked by red) and OM external clay mineral (marked by blue) in sample X3, the proportions of OM external clay in sample X3 is 89.6%; (e) Distribution of pyrite and quartz sample X4; (f) Abundant existence of clay mineral in OM (marked by red) and OM external clay mineral (marked by blue) in sample X4, the proportions of OM external clay in sample X4 is 82.9%.

In summary, the water content of the four shale samples increased gradually with the increase of RH. However, the water

adsorption behaviors of shale samples in different RH stages were different, and there were also differences among different samples.

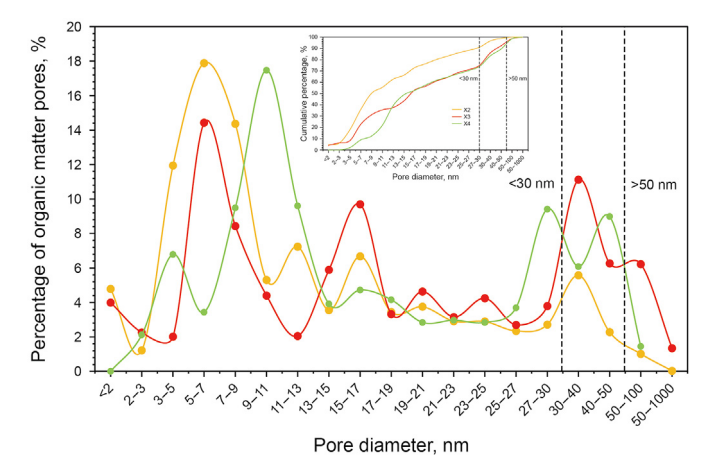
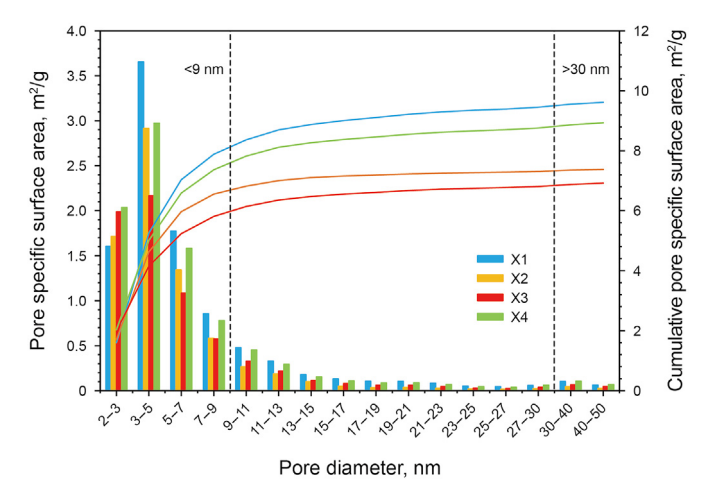


Fig. 5. OM pore diameter distribution obtained by IPP software using FE-SEM images.



**Fig. 6.** The specific surface area distribution of Longmaxi Formation shale samples. The mesopores are determined from N2 adsorption data and the macropores are from HPMIP (high pressure mercury intrusion porosimetry) data.

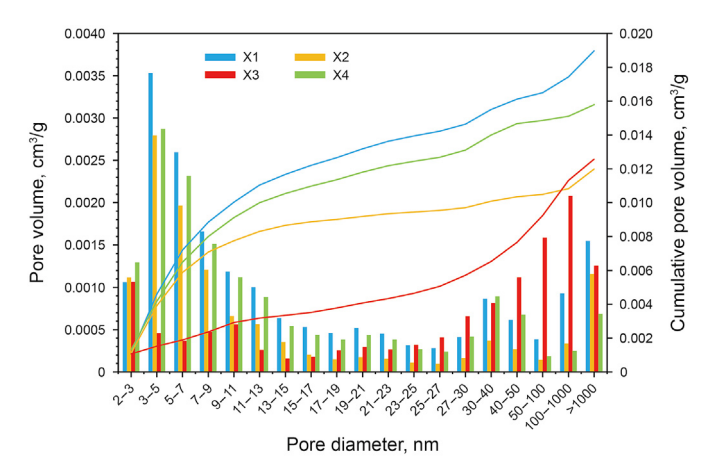


Fig. 7. The pore volume distribution of Longmaxi Formation shale samples. The mesopores are determined from  $N_2$  adsorption data and the macropores are from HPMIP (high pressure mercury intrusion porosimetry) data.

#### 4. Discussion

#### 4.1. The effect of pore structure on water content of shale samples

Previous studies have shown that the main mechanism influencing water adsorption process is the competitive occupation of adsorption sites in shale samples, so it is very important to investigate the influence of the specific surface area on shale water content (Rexer et al., 2013; Liang et al., 2016; Chen et al., 2019; Zhu et al., 2021).

As shown in Fig. 10a, there was no good correlation between the BET-specific surface area and the TOC content of shale samples, but there was a good correlation between the clay minerals-normalized BET specific surface area and the TOC content ( $R^2 = 0.94$ ). As shown in Fig. 10b, the BET-specific surface area and the clay content of shale samples did not show a good correlation. However, there was a good correlation between the TOC-normalized BET-specific surface area and the clay content ( $R^2 = 0.96$ ), indicating that OM and clay minerals jointly controlled the specific surface area of these shale samples. As shown in Fig. 11a, there was a poor relationship between the water content and the BET-specific surface area, which is because the OM and clay minerals with different affinities to water jointly controlled the specific surface area. With the increase of RH, water molecules adsorbed on the clay minerals and OM no longer occurred in a monolayer adsorbed state (Li et al., 2021). And when the RH reached 99%RH, a large number of water molecules in the pore spaces occurred in a multilaver adsorption and capillary condensed state (Li et al., 2017). Therefore, the four shale samples showed a good correlation between water content and porosity at 99%RH state (Fig. 11b).

# 4.2. The effect of clay minerals and OM on water content of shale samples

The water content of shale samples showed a good correlation with the clay content and this correlation was gradually weakened with the increase of RH (Fig. 12). The slope of the trend line in Fig. 12 showed the water adsorption capacity of clay minerals.

When the RH was 16%RH, the slope was low and the Y-intercept was approximately 0. Clay minerals provided almost all the water adsorption capacity of shale samples, but water molecules mainly entered the interlayer pores of clay minerals at this stage, so the water adsorption capacity of clay minerals was quite limited.

When the RH was 16%RH~41%RH, the slope increased slightly and the Y-intercept also increased. This indicated that the water adsorption capacity of clay minerals increased weakly and water molecules gradually changed from monolayer adsorption to multilayer adsorption on the surface of clay minerals at this stage. Furthermore, other components besides clay minerals began to adsorb water molecules at this stage.

When the RH was 41%RH ~99%RH, the slope gradually increased, and the water adsorption capacity of clay minerals increased rapidly at this stage. Water molecules gradually changed from the multilayer adsorption state to condensed state in the clay mineral pores. The continuous increase in the Y-intercept indicated that other components continued to adsorb water molecules at this stage.

The relationship between water content and TOC content at different RHs was also investigated as shown in Fig. 13. The Y-intercept of the trend line gradually increased with the increase of

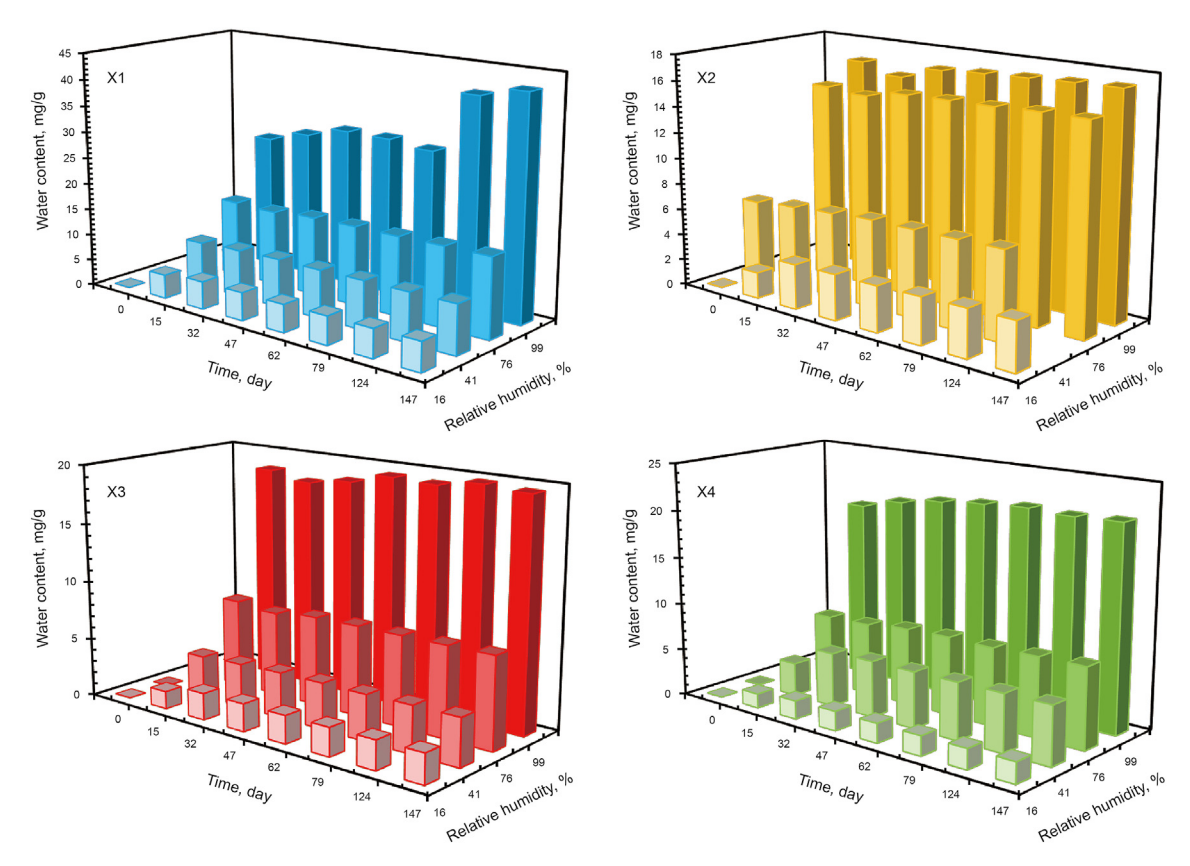


Fig. 8. Experimental results for the water adsorption process of shale samples.

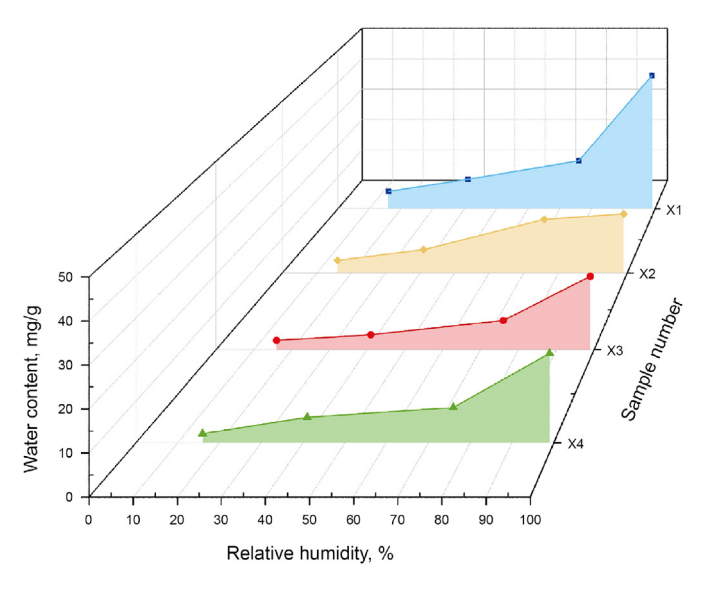


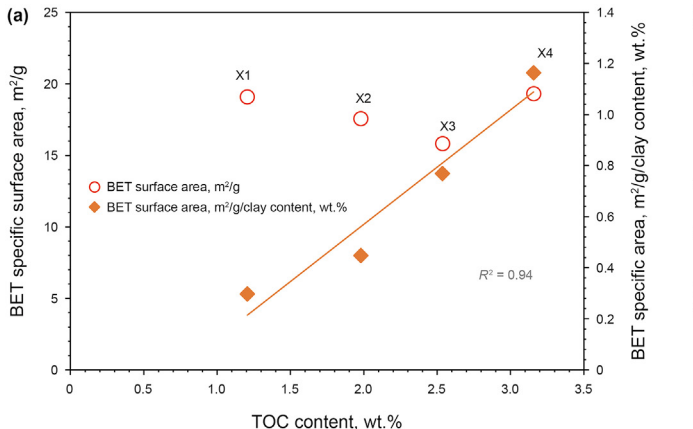
Fig. 9. The relationship between water content and the RH of shale samples.

RH, indicating that the water adsorption capacity of other components (possibly clay minerals) gradually increased. When the RH was 16%RH, the slope was negative, indicating that the OM began to delay the water adsorption capacity of shale at this stage. When the RH was 16%RH ~41%RH, the slope decreased weakly, indicating that the delayed effect of OM on water adsorption capacity increased weakly at this stage. When the RH was 41%RH ~99%RH, the slope decreased gradually, indicating that the delayed effect of OM on water adsorption capacity increased rapidly at this stage.

It is worth noting that previous studies have shown that OM has the ability of adsorbing water molecules (Gu et al., 2016; Kuila et al., 2014; Bai et al., 2021). In order to better clarify the water adsorption capacity of OM, the water content was normalized for clay content, as shown in Fig. 14. When the RH was 16%RH, the slope was about 0, and the OM hardly provided any water adsorption capacity at this stage. When the RH was 16%RH~41% RH, the slope increased rapidly and the OM began to adsorb water molecules. At this stage, the water molecules began to be adsorbed by the oxygen-containing functional groups of the OM in the monolayer adsorption state. When the RH was 41%RH~76%RH, the slope remained unchanged. At this stage, a large number of water molecules continued to be adsorbed by OM in the monolayer adsorption state. When the RH was 76%RH~99%RH, the slope gradually increased and the water adsorption capacity of OM was enhanced. At this stage, water molecules were gradually transformed into water cluster forms in OM pores. In summary, OM indeed made the contribution to the water adsorption capacity, but more importantly OM played the role of delaying the water adsorption capacity of shale samples.

## 4.3. The distribution of water molecules in the pore spaces of shale samples

In the water adsorption process of shale samples, water molecules preferentially occupy the small clay mineral pores and gradually occupy large pores with the increase of water content (Li et al., 2016). Water vapor adsorption curve can be used for pore structure characterization (Hagymassy et al., 1969) according to the Kelvin equation (Fisher et al., 1981) (Eq. (1)).



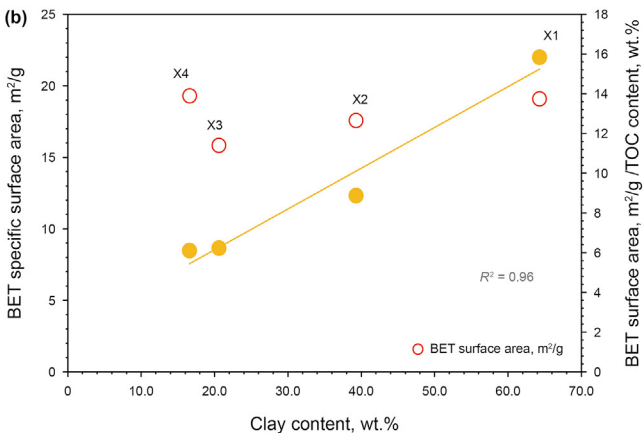
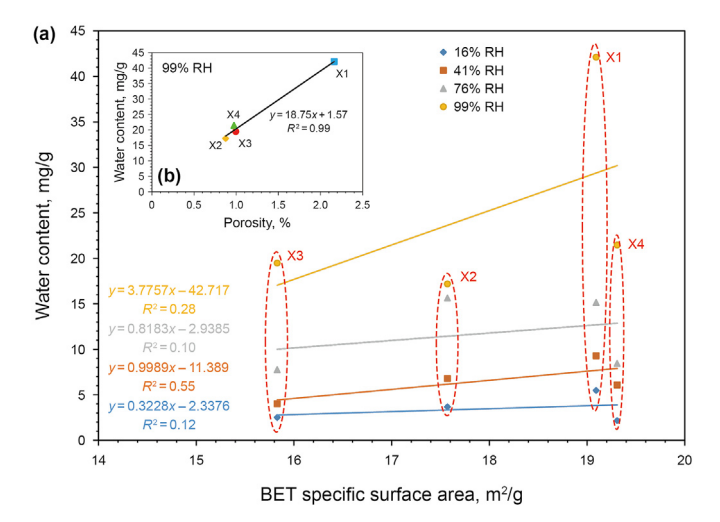
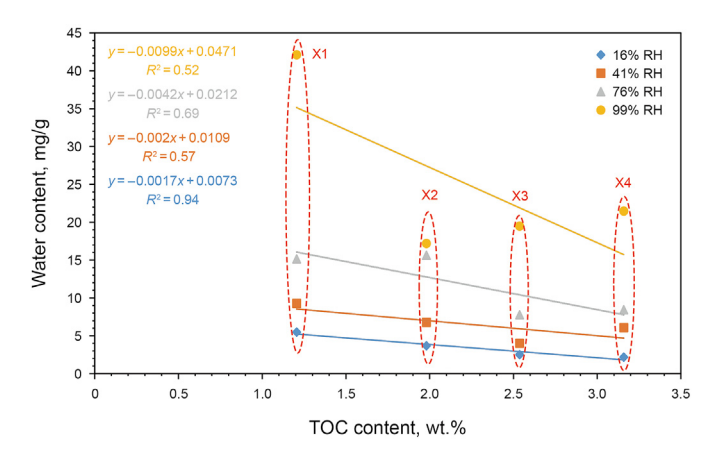


Fig. 10. The relationships between the BET specific surface area and the total organic carbon (TOC) content (wt.%) and clay content (wt.%); the clay content-normalized BET surface area and TOC content (wt.%); and the TOC-normalized BET surface area and clay content (wt.%).



**Fig. 11.** The relationship between the BET-specific surface area and the water content of shale samples.



 ${f Fig.~13.}$  The relationship between the OM content and the water content of shale samples.

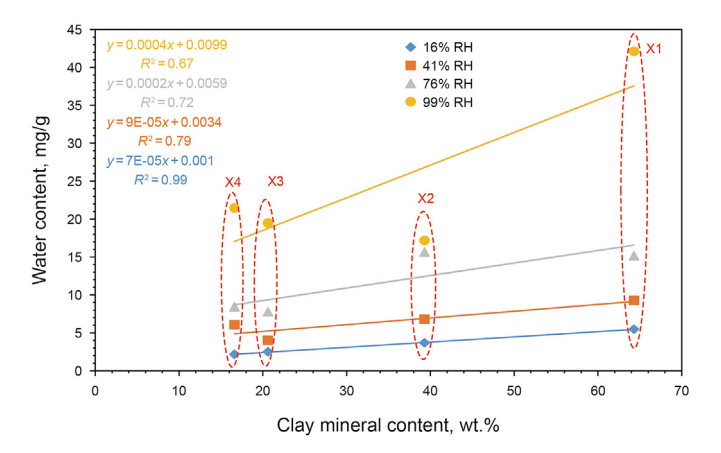


**Fig. 12.** The relationship between the clay mineral content and the water content of shale samples.

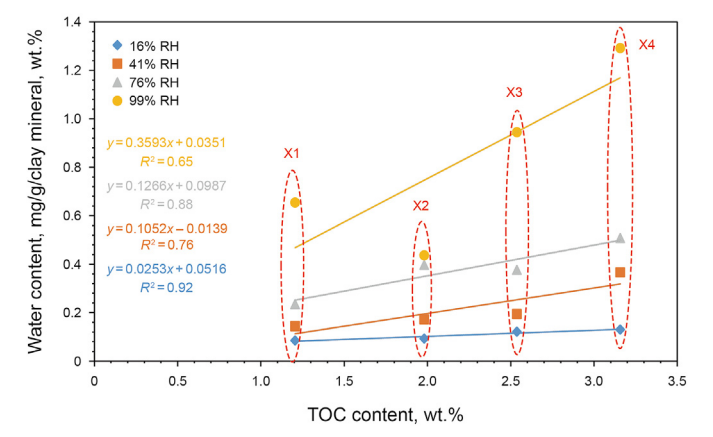


**Fig. 14.** The relationship between the OM content and the clay mineral-normalized water content of shale samples.

**Table 1**Relationship between RH and pore diameter.

RH, %	16	41	76	99
Calculated pressure, MPa	249.81	121.55	37.43	1.37
Calculated diameter, nm	1.1	2.5	7.7	212.0

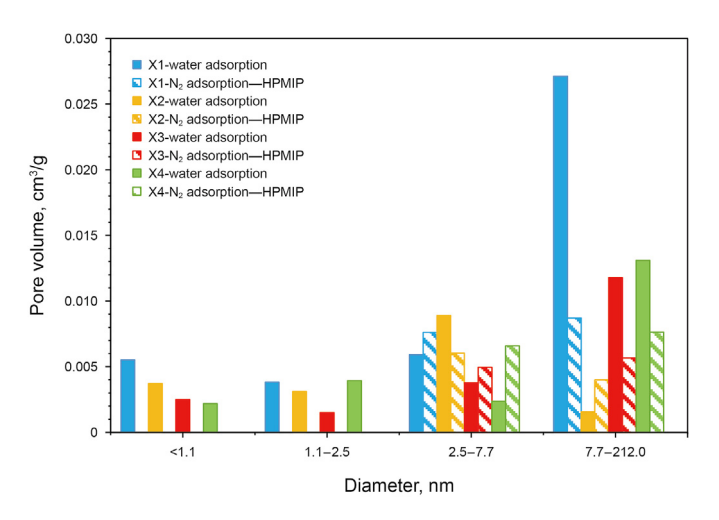


Fig. 15. The pore diameter distribution of water adsorption experiment,  $N_2$  adsorption experiment and high-pressure mercury injection experiment (HPMIP) were used to jointly characterize the pore size distribution.

$$\operatorname{Ln}\frac{P}{P_0} = -\frac{2\gamma M}{RT\rho} \times \frac{1}{r} \tag{1}$$

where  $P/P_0$  is the RH,  $\gamma$  is the surface tension, M is the molar mass of the liquid, R is the gas constant, T is the isothermal temperature (absolute),  $\rho$  is the density of the liquid, and r is the mean radius of curvature of the liquid/gas interface with temperature T.

The calculated pore sizes corresponding to different RHs are presented in Table 1 and the pore volumes with different diameters were obtained as shown in Fig. 15. Due to the presence of a large number of pores in shale samples that water molecules can enter but nitrogen molecules could not (such as interlayer pores of clay minerals) (Yang et al., 2020a, 2020b), the distribution of water molecules in the pores of shale samples was discussed by combining the processes of water adsorption and nitrogen adsorption.

Fig. 15 shows the pore diameter distribution of four shale samples obtained from water adsorption, N<sub>2</sub> adsorption and HPMIP tests. When the RH was 76%RH ~99%RH, water molecules occupied the largest pore volume for samples X1, X3 and X4 and the pores occupied by water ranged from 7.7 nm to 212.0 nm. While X2 had the smallest pore volume occupied by water molecules at 76%RH ~99%RH and the largest pore volume occupied by water molecules at 41%RH~76%RH.

The proportion of OM pores with diameter of 7.7–212.0 nm in sample X2 was 61.01%— lower than that in sample X3 (76.96%) and sample X4 (88.79%). However, the proportion of OM pores with diameter of 2.5–7.7 nm (41%RH ~ 76%RH) in sample X2 was 38.98%—much larger than that of sample X3 (22.75%) and sample X4 (11.08%). Consequently, the pore volume difference between sample X2 and X3, X4 indicated from water adsorption at 41%RH ~76%RH and 76%RH ~99%RH showed a similarity to the OM pore difference between sample X2 and X3, X4, which indicated the considerable contribution of OM pores to the water adsorption capacity of shale samples when the RH was higher than 41%RH.

When the RH was 41%RH~76%RH (2.5–7.7 nm), water molecules could only be adsorbed by the oxygen-containing functional groups on the surface of OM besides clay minerals, so the adsorption capacity of water molecules was lower than that of nitrogen molecules which covered all the pore surfaces in shale. Therefore, samples X1, X3 and X4 all showed that the pore volume occupied by water molecules was lower than that occupied by nitrogen molecules. As to sample X2 with a greater number of smaller OM pores, water molecules tended to transform from the monolayer adsorption state to water clusters in smaller OM pores and water molecules started to be adsorbed by OMs surrounded by clay minerals. Consequently, the water molecules occupied a larger pore volume than nitrogen molecules. When the RH increased to 76%RH ~99%RH (7.7 nm-212.0 nm), X1, X3 and X4 all showed that water molecules occupied a larger pore volume than that occupied jointly by  $N_2$  (7.7 nm-50nm) and Hg (50 nm-212nm). During this RH range, water molecules started to transform from the monolayer adsorption state into the water cluster state in the OM pores and gradually entered the interlayer pores of clay minerals in OM.

Different from the other three samples, while water molecules occupied a smaller pore volume than that occupied jointly by  $N_2$  and Hg for sample X2 at 76%RH ~99%RH, which is because the pore volume of 7.7–212 nm measured by combined  $N_2$  adsorption and HPMIP was much larger than the pore volume indicated from water adsorption at this pore size range due to the ink-bottle effect of HPMIP test (Gao et al., 2018; Zhang et al., 2019).

#### 4.4. The water adsorption process of shale samples

#### 4.4.1. The three stages of water adsorption process

This study mainly considered the influence of clay minerals and OM on the water adsorption process of shale due to the controlling effect of OM together with clay minerals on the specific surface area. The water adsorption process of shale samples is divided into three stages based on the water adsorption characteristics of clay minerals and OM (Fig. 16).

4.4.1.1. Stage (1): 0%RH~16%RH. At this stage, the interlayer pores of the OM external clay minerals acted as preference entrance for water molecules, which did not enter the OM pores. Since only interlayer pores of clay minerals can provide water adsorption capacity at this stage, the water adsorption capacity of shale samples at this stage was limited.

4.4.1.2. Stage (2): 16%RH~41%RH. At this stage, the adsorption mechanism of water molecules gradually transformed from monolayer adsorption to multilayer adsorption on the surface of clay minerals. And OM with adsorption sites of oxygen-containing functional groups started to adsorb water molecules.

4.4.1.3. Stage (3): 41%RH~99%RH. At this stage, the water adsorption capacity of clay minerals increased rapidly, and water molecules gradually changed from the multilayer adsorption state to condensed capillary water state and were present in the clay mineral pores. When the RH was 41%RH~76%RH, a large number of water molecules continued to adsorb on the oxygen-containing functional groups of OM pores in the monolayer adsorption state. When the RH was higher than 76%RH, water molecules were gradually transformed into the water cluster form and adsorbed on the surface of the oxygen-containing functional groups of OM pores. The RH conversion point of water molecules from monolayer adsorption to water cluster adsorption was related to the pore diameter of OM pores. Shale samples with a larger amount of smaller OM pores began the transformation of the monolayer adsorption state to the water cluster adsorption state when the RH

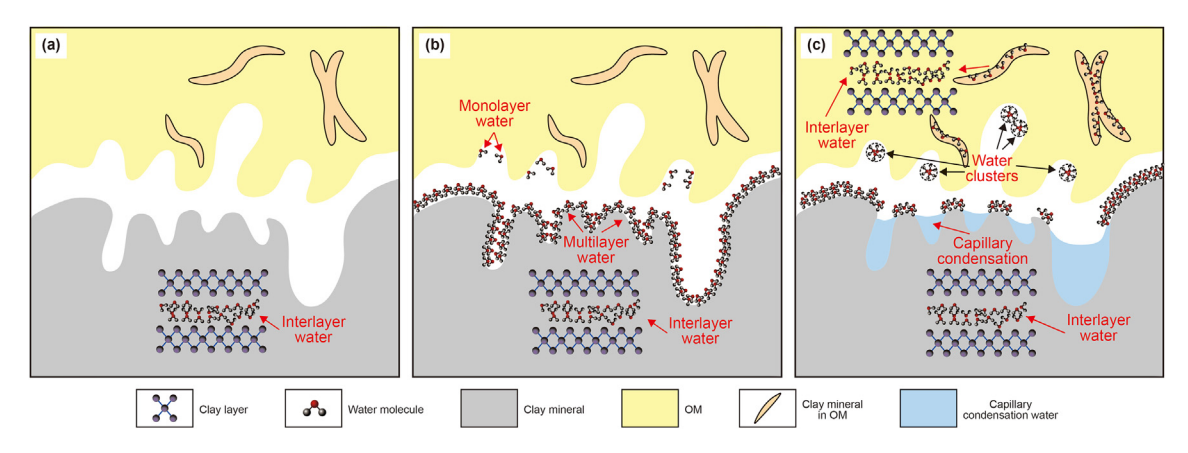


Fig. 16. Water adsorption process of shale samples in different RH stages.

was low. With the continuous increase of RH, water molecules gradually entered the interlayer clay mineral pores within OM. Finally, when the RH reached 99%RH, a large number of water molecules were condensed in the pore spaces owing to capillary force.

#### 4.4.2. The theoretical calculation of water adsorption process

Previous studies have shown that several classical adsorption models (GAB, DLP, OSWIN, Freundlich, and FHH) can be used to describe the water adsorption process of Longmaxi Formation shale, but different models have slight differences (Shen et al., 2019; Yang et al., 2021). According to the different occurrence states of water molecules on the surface of shale pores in the three stages, different theoretical models were used to analyze the water adsorption behavior of shale samples under different RHs.

In stage (1), the interlayer clay mineral pores play the role of preferential channel for the entrance of water molecules, thus, almost no water molecules entered the OM pores. The clay minerals in the Longmaxi Formation shale samples from the Southern Sichuan Basin were dominated by illite and illite-smectite (I/S) mixed layers, and the proportion of illite and I/S in the clay minerals are generally high (Wang et al. 2015, 2020; Huang et al., 2020). The content ratio of illite to smectite in the I/S mixed layers increased with burial depth, but it tended to be stable when the ratio reached 4:1 (Weaver, 1989). Due to the high thermal evolution of the Longmaxi Formation shale (Dai et al., 2014; Wang et al., 2019; Zhang et al., 2020), the clay minerals were assumed to be with a ratio of illite and I-S mixed layers (I/S = 4:1) of 1:1 for the convenience of calculation, and the ratio of the illite content to the smectite content was 9:1. Since illite has no inner surface and K<sup>+</sup> is embedded in the pores of the silica layer inside the clay mineral, the small hydration effect of K<sup>+</sup> makes it difficult for water molecules to enter the interlayer of illite. On the other hand, smectite has a three-layer structure. The interlayer force between the crystal

layers is very small, and the interlayers can easily accept the water molecules (Zhang et al., 2020). Therefore, the inner surface area of the smectite crystal layer is calculated according to equation (2).

$$M_1 = A_s \times H_{\text{mono}} \times \rho_w \times \rho_s \times w \ (clay)$$
 (2)

where  $M_1$  is the theoretical water adsorption of clay minerals in stage (1) mg<sub>water</sub>/g<sub>shale</sub>;  $A_s$  is the internal surface area of montmorillonite, at 750 m²/g (data from Passey et al., 2013);  $H_{\rm mono}$  is the thickness of water molecules adsorbed by the monolayer, at 0.3 nm (from Johnston's clay mineral interlayer pore structure measurement (Johnston, 2010);  $\rho_{\rm w}$  is the density of water at the experimental temperature (35 °C), at 0.9941 × 10³ kg/m³;  $\varphi_{\rm s}$  is the smectite content in the clay minerals, at 10%; and w (clay) is the clay mineral content, in wt.%.

As fitting parameters at stage (1) shown in Table 2, the theoretical water adsorption is in a good correlation with the actual water adsorption, and is greatly larger than the experimental water adsorption results. The good correlation ( $R^2 = 0.99$ ) indicates that the interlayer pores of clay minerals contribute the main adsorption space for water molecules at this stage but only part of the interlayer pores of clay minerals could provide water adsorption sites.

In stage (2), water molecules gradually changed from monolayer adsorption to multilayer adsorption forms on the surface of clay minerals. Therefore, the multilayer Freundlich model (FM) (Eq. (3)) was used to analyze the water adsorption behavior of shale samples in stage (2) (Hatch et al., 2012).

$$LnM_2 = LnA + \frac{1}{B} \times Ln(RH) \tag{3}$$

where  $M_2$  is the theoretical water adsorption of shale samples in stage (2) mg<sub>water</sub>/g<sub>shale</sub>; A represents the parameters related to the water adsorption capacity; B represents the parameters referring to

**Table 2** Fitting parameters of each RH stage.

	Stage(1)		Stage(2)		Stage(3)		
	M <sub>1</sub> , mg/g	M <sub>1</sub> , mg/g	A	В	C	D	Е
X1	14.38	5.48	18.08	1.45	5.54	-3.36	0.14
X2	8.79	3.67	20.93	0.89	2.84	-1.16	1.94
X3	4.61	2.50	9.54	1.19	3.43	-2.12	0.33
X4	3.71	2.17	10.67	1.33	27.09	-25.29	0.01
Equation	$M_1 = 0.84 \times M_1 +$	$0.001 (R^2 = 0.99)$	Freundlich		Dubinin-Asta	akhov	

**Note:**  $M_1$  is the theoretical water adsorption, and  $M_1$  is the actual water adsorption.

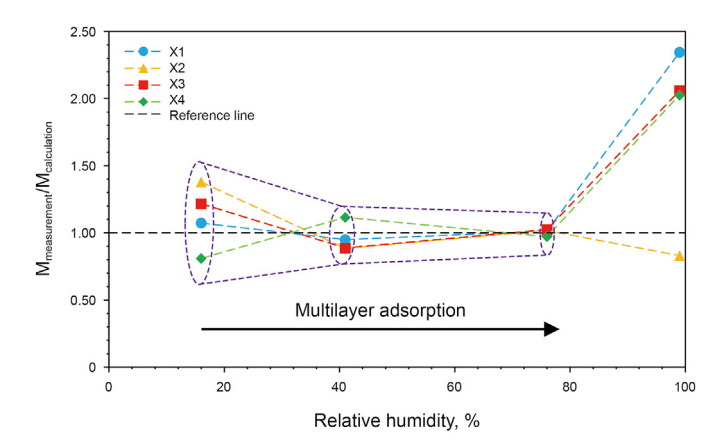


**Fig. 17.** The relationship between the measured water content conditions and the theoretical value of the Freundlich model under different RH conditions.

the water adsorption strength between shale and water molecules; and RH is the relative humidity.

The parameters in Freundlich water adsorption model are shown in Table 2. Value A of samples X1 and X2 was larger than samples X3 and X4, which was because the clay content of samples X1 and X2 was much larger than samples X3 and X4. Clay minerals in shale provided the main water molecule adsorption space, so the parameters of samples X1 and X2 related to the water adsorption capacity were larger. Due to the larger number of smaller OM pores in sample X2, the OM pores in sample X2 began to adsorb water in stage (2). However, the interaction strength between OM and water molecules was much weaker than that between clay minerals and water molecules, so the value B of sample X2 was smaller. As shown in Fig. 17, with the increase of RH, water molecules gradually occurred in the multilayer adsorption state  $(M_{measurement}/M_{calcula-})$ tion gradually tended to be 1). However, the Freundlich model could not reflect the high RH conditions, where the water molecules in the multilayer adsorption state were transformed into the capillary condensed state.

In stage (3), the adsorption mechanism of water molecules is gradually transformed from the multilayer adsorption to capillary condensation in the clay mineral pores and monolayer adsorption to water clusters on the surface of oxygen-containing functional groups in the OM pores. Therefore, the Dubinin–Astakhov model (DAM) (Eq. (4)) was used to analyze the water adsorption behavior of shale samples in stage (3) (Feng et al., 2018).

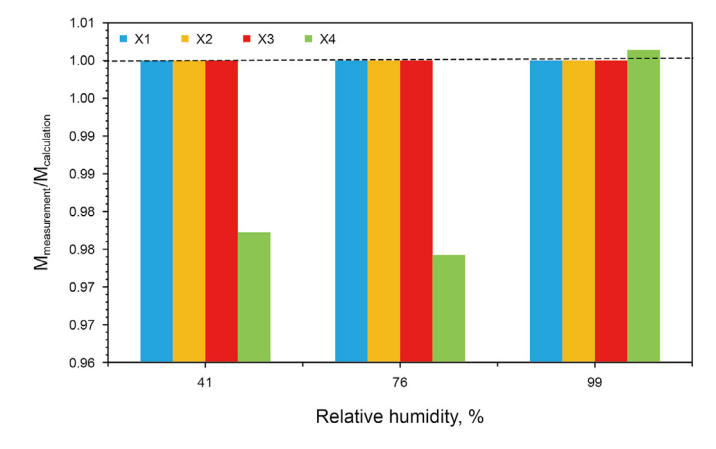


**Fig. 18.** The relationship between the measured water content and theoretical value of the Dubinin–Astakhov model (DAM) under different RH conditions.

$$LnM_3 = C + D \times \left(Ln\frac{1}{RH}\right)^E \tag{4}$$

where  $M_3$  is the theoretical water adsorption of shale samples in stage (3)  $\mathrm{mg_{water}}/\mathrm{g_{shale}}$ ;  $C = \mathrm{LN}_{M_{\mathrm{max}}}$ , and  $M_{\mathrm{max}}$  is the maximum water adsorption content; D represents the parameters related to the adsorption energy; E represents the parameters related to the heterogeneity of shale samples.

The parameters in DAM are also shown in Table 2. The calculated water content using the DAM and the measured water content under different RH conditions are shown in Fig. 18. The DAM could describe the water content of samples X1, X2 and X3. The value C of sample X1 was obviously higher than that of samples X2 and X3, which was because of its highest clay content —the main contributor to water adsorption capacity. The parameter D is in the order of D1 > D3 > D2, indicating that X1 had the maximum water adsorption capacity and X2 had the minimum water adsorption capacity. Water molecules were firstly adsorbed on hydrophilic adsorption sites with high energy (Ramachandran et al., 2006) and the clay minerals in sample X1 adsorbed more water through pores. Sample X2 had the lowest water adsorption capacity due to its large number of smaller OM pores and more water molecules were adsorbed on the surface of OM pores. In summary, existing models are better at characterizing shale samples with more clay content and more small OM pores. However, for sample X4, a shale sample with lower clay content and fewer small OM pores, the water adsorption behavior could not be well described by these models.

#### 4.4.3. The modification of water adsorption model of shale samples

As mentioned above, most of the existing models are based on the pore structure of shale, and the fitting results are poor. When the RH is low (stages (1) and (2)), due to the wettability differences between clay minerals and OM, water molecules show preferential adsorption on clay mineral pores while the existing models do not consider the different effects of OM and clay minerals on the water adsorption ability of shale or the influence of the clay mineral occurrence state (in OM or outside of OM). Therefore, this study modified the existing water adsorption models of shale samples considering the differences of OM and clay minerals and the influence of clay mineral occurrence state.

The proportions of clay minerals in OM and outside of OM were determined by using IPP software to identify clay minerals at different locations in FE-SEM images. The proportion of clay minerals outside of OM in samples X2, X3 and X4 was 0.651881, 0.485453 and 0.457924, respectively.

In stage (1), there was the water adsorption capacity of clay minerals being considered at this stage on account of the main contribution of the clay mineral interlayer pores. And the low RH model (LRHM) was proposed as Eq. (5).

4.4.3.1. Stage (1):0 < RH < 0.16.

$$M_{water} = A_1 \times [w(clay) \times w(clay minerals outside of OM)]^{B_1 \times (1-RH)}$$
(5)

where w (clay) is the clay mineral content (wt.%) and w (clay minerals outside of OM) is the content of clay minerals outside of OM (wt.%).

In stage (1) of this study, the fitting  $A_1$  and  $B_1$  values of X2, X3 and X4 samples are 6.5586 and 0.5049, respectively, and the  $R^2$  is 0.99

In stage (2), water molecules gradually changed from a

**Table 3** Fitting parameters in stage (2).

Pore diameter, nm	$A_2$	B <sub>2</sub>	$C_2$	$R^2$
3-5	0.0087	-2.9503	104.4671	0.77
5-7	0.0158	-2.1041	43.6599	0.76
7-9	0.0155	-2.1202	31.8085	0.77
9-11	0.0243	-1.2141	34,2831	0.80
11-13	0.3699	4.6324	48.6898	0.91
13-15	0.2800	3.8369	40.7361	0.91
15-17	0.2928	3.9882	40.6303	0.91
17-19	0.2953	3.9461	33.1644	0.89
19-21	0.2901	3.8829	30.8222	0.88
21-23	0.2881	3.8569	29.4005	0.88
23-25	0.2862	3.8242	27.8678	0.88
25-27	0.2830	3.7876	26.7810	0.87
27-30	0.2789	3.7362	25.4439	0.87
30-40	0.2682	3.5888	22.3771	0.87
40-50	0.2610	3.4883	20.8494	0.87
50-100	0.2503	3.3353	19.2105	0.85
100-1000	0.2488	3.3102	18.9346	0.85

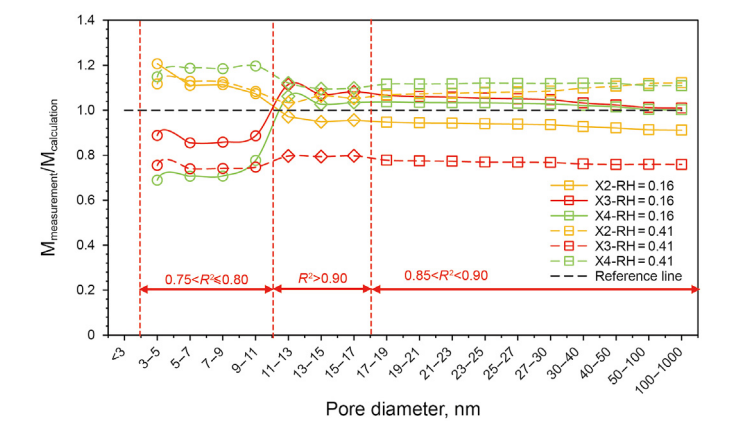


Fig. 19. The relationship between the measured water content in different pore diameters and the theoretical value of the model.

monolayer adsorption state to multilayer adsorption state on the surface of clay minerals, and were adsorbed by the oxygen functional group sites on the surface of OM pores occurred in the monolayer adsorption state. With the increase of RH, water molecules gradually took precedence over smaller OM pores in the form of water clusters. In order to clarify the pore diameter range in which water molecules preferentially occurred as water clusters, the OM pore proportion within the full pore diameter range was used to calculate the water content of shale samples. Since the proportion of OM pores less than 3 nm in sample X4 was 0, only OM pores larger than 3 nm were counted considering the practicality. And then the medium RH model (MRHM) was proposed as Eq. (6). The fitting parameters are listed in Table 3 and the fitting results are shown in Fig. 19.

4.4.3.2.  $Stage(2):0.16 \le RH \le 0.41$ .

$$\begin{array}{l} M_{water} \! = \! A_2 \times [w(clay) \times w(clay\,minerals\,outside\,of\,OM)]^{B_2 \times (1+RH)} + \\ \{C_2 \times [w(TOC) \times w(P_o)]\}^{RH} \end{array}$$

where w (clay) is the clay content (wt.%); w (clay minerals outside of OM) is the content of clay minerals outside of OM (wt.%); w (OM) is the TOC content (wt.%); w( $P_o$ ) is the proportion of OM pores.

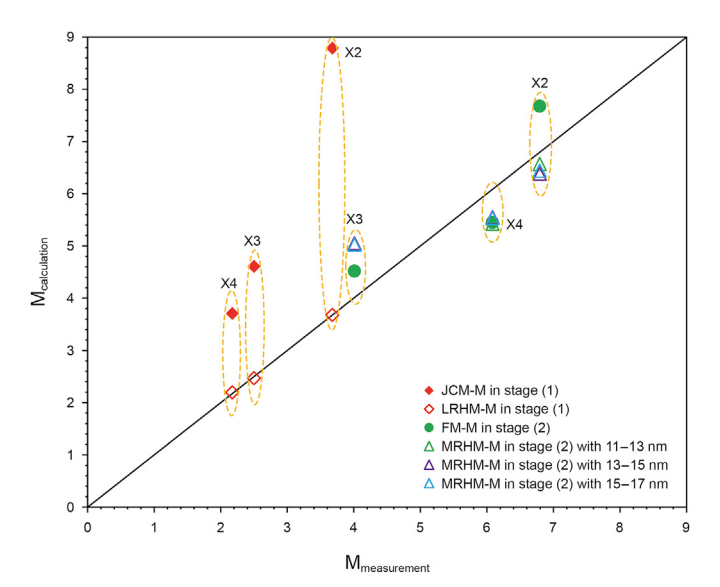


**Fig. 20.** The relationship between the measured water content and the theoretical value of the different models in stage (1) and stage (2).

 $B_2$  is a negative number in small pores (3–11 nm) but a positive number in large pores (>11 nm), which indicated the competitive adsorption between small OM pores and clay mineral pores outside of OM. With the increase of OM pore size, the competition no longer plays an important role. Since the value of  $C_2$  was the largest in the small OM pore diameter range (3–5 nm) and decreased gradually with the increase of the pore diameter, which indicated that water molecules were preferentially adsorbed by the small OM pores. The fitting result of MRHM in OM pores with a pore diameter range of 11–17 nm showed a good correlation, which might be caused by the high specific surface area of OM pores between 11 and 17 nm of samples X2, X3 and X4.

As shown in Fig. 20, the fitting results of LRHM in stage (1) and MRHM in stage (2) are better than the fitting results of JCM in stage (1) and FM in stage (2). The ignorance of different spatial configuration relationship between OM and clay minerals in JCM leads to the results that the calculated water contents of ICM are obviously higher than the measured values in the low RH stage (stage 1). However, FM has limitations in the presentation of competitive adsorption which water molecules preferentially entered clay mineral pores outside of OM and small OM pores in the medium RH stage (Stage 2). In addition, it should be noted that the fitting result of MRHM of sample X3 in stage (2) is weaker than the FM. The wettability of the carbonate minerals altered to be hydrophobic during the thermal evolution of OM (Legens et al., 1998), and the abundant existence of carbonate minerals in X3 probably delayed the entrance of water molecules in pore spaces during stage (2). Most water molecules were eventually adsorbed in all the hydrophilic sites in shale pore structure and existed in a condensed state. Therefore, DAM could describe the water adsorption capacity of shale well in high RH stage (stage 3) because there was gradually less (or no) competitive adsorption between different components. In general, it is of great significance to divide water adsorption stages and modify equations to fit water adsorption in different RH stages.

#### 5. Conclusion

This study investigated the water adsorption characteristics of Longmaxi Formation shale samples under four different RH conditions and the controlling factors. The OM-clay complexes were

(6)

commonly observed in these Longmaxi Formation shale samples, which significantly affected the water adsorption process of shale samples. The water adsorption process of Longmaxi Formation shale under different RH conditions was divided into three stages and the modified LRHM and MRHM models considering the spatial configuration relationship between OM and clay minerals were proposed to describe the first two water adsorption stages while the DAM model was used to fit the third water adsorption stage. In stage (1), water molecules preferentially entered the interlayer pores of clay minerals outside of OM, and almost no water molecule entered the OM pores. In stage (2), water molecules were gradually transformed into multilayer adsorption forms on the surface of clay minerals, and OM with oxygen-containing functional groups provided adsorption sites for the monolayer adsorption of water molecules. In stage (3), the water adsorption capacity of clay minerals increased rapidly, and water molecules gradually changed from the multilayer adsorption state to condensed state in the clay mineral pores. Water molecules were gradually transformed into water clusters and adsorbed on the surface of the adsorption sites of oxygen-containing functional groups in the OM pores. The RH conversion point of water molecules from monolayer adsorption to water clusters was related to the pore diameter of OM pores. Shale samples with more small OM pores began the transformation at lower RH. With a continuous increase of RH, water molecules gradually entered the clay mineral pores in OM.

It should be noted that the modified equations in this study were based on the differences of clay content, TOC content and pore structure. However, in the actual water adsorption process of shale, the thermal maturity and clay mineral type as well as the kerogen type, may all affect the water adsorption process of shale.

#### Acknowledgements

This research was supported by the National Natural Science Foundation of China (No. 41972145), National Science and Technology Major Project of China (No. 2017ZX05035—002), the Foundation (No. PRP/indep-2-1904, PRP/indep-3-1707 and No. PRP/indep-3-1615) of State Key Laboratory of Petroleum Resources and Prospecting from China University of Petroleum in Beijing, as well as fundamental Research Funds for China University of Geosciences under Award Number 35832019035. Yu Cheng and Yupeng Fan are acknowledged for their help in data acquisition for the water adsorption experiment and pore structure analysis.

#### References

- Bai, J., Kang, Y., Chen, M., et al., 2021. Impact of water film on methane surface diffusion in gas shale organic nanopores. J. Petrol. Sci. Eng. 196 (2021), 108045. https://doi.org/10.1016/j.petrol.2020.108045.
- Chalmers, G., Bustin, M., 2010. The effects and distribution of moisture in gas shale reservoir systems. AAPG ACE 11–14.
  Chen, J., Gai, H.F., Xiao, Q.L., 2021. Effects of composition and temperature on water
- Chen, J., Gai, H.F., Xiao, Q.L., 2021. Effects of composition and temperature on water sorption in overmature Wufeng-Longmaxi shales. Int. J. Coal Geol. 234, 103673. https://doi.org/10.1016/j.coal.2020.103673.
- Chen, L., Jiang, Z.X., Liu, Q.X., et al., 2019. Mechanism of shale gas occurrence: insights from comparative study on pore structures of marine and lacustrine shales. Mar. Petrol. Geol. 104, 200–216. https://doi.org/10.1016/j.marpetgeo.2019.03.027.
- Cheng, P., Tian, H., Xiao, X.M., et al., 2017. Water distribution in overmature organic-rich shales: implications from water adsorption experiments. Energy Fuel. 31 (12), 13120—13132. https://doi.org/10.1021/acs.energyfuels.7b01531.
- Cheng, P., Xiao, X.M., Tian, H., et al., 2018. Water content and equilibrium saturation and their influencing factors of the lower paleozoic overmature organic-rich shales in the upper yangtze region of southern China. Energy Fuel. 32 (11), 11452–11466. https://doi.org/10.1021/acs.energyfuels.8b03011.
- Cicchino, A.M.P., Sargent, C., Goulty, N.R., et al., 2014. Regional variation in Cretaceous mudstone compaction trends across Haltenbanken, offshore mid-Norway. Petrol. Geosci. 21 (1), 17–34. https://doi.org/10.1144/petgeo2014-035.
- Dai, J.X., Zou, C.N., Liao, S.M., et al., 2014. Geochemistry of the extremely high thermal maturity Longmaxi shale gas, southern Sichuan Basin. Org. Geochem.

74, 3-12. https://doi.org/10.1016/j.orggeochem.2014.01.018.

- Fang, C.H., Huang, Z.L., Wang, Q.Z., et al., 2014. Cause and significance of the ultralow water saturation in gas-enriched shale reservoir. Nat. Gas Geosci. 25 (3), 471–476. https://doi.org/10.11764/j.issn.1672-1926.2014.03.0471 (in Chinese).
- Feng, D., Li, X.F., Wang, X.Z., et al., 2018. Water adsorption and its impact on the pore structure characteristics of shale clay. Appl. Clay Sci. 155, 126–138. https:// doi.org/10.1016/j.clay.2018.01.017.
- Fisher, L.R., Gamble, R.A., Middlehurst, J., 1981. The Kelvin equation and the capillary condensation of water. Nature 290 (5807), 575–576. https://doi.org/10.1038/290575a0.
- Gao, Z.Y., Fan, Y.P., Hu, Q.H., et al., 2020. The effects of pore structure on wettability and methane adsorption capability of Longmaxi Formation shale from the southern Sichuan Basin in China. AAPG (Am. Assoc. Pet. Geol.) Bull. 104 (6), 1375–1399. https://doi.org/10.1306/01222019079.
- Gao, Z.Y., Hu, Q.H., 2018. Pore structure and spontaneous imbibition characteristics of marine and continental shales in China. AAPG (Am. Assoc. Pet. Geol.) Bull. 102 (10), 1941–1961. https://doi.org/10.1306/03291817297.
- Gao, Z.Y., Hu, Q.H., Hamamoto, S., 2018. Using multicycle mercury intrusion porosimetry to investigate hysteresis phenomenon of different porous media. J. Porous Media 21 (7), 607–622. https://doi.org/10.1615/JPorMedia.2018017822.
- Ge, H.K., Yang, L., Shen, Y.H., et al., 2015. Experimental investigation of shale imbibition capacity and the factors influencing loss of hydraulic fracturing fluids. Petrol. Geosci. 12 (4), 636–650. https://doi.org/10.1007/s12182-015-0049-2.
- Ghanbari, E., Dehghanpour, H., 2016. The fate of fracturing water: a field and simulation study. Fuel 163, 282–294. https://doi.org/10.1016/j.Fuel.2015.09.040.
- Goulty, N.R., Sargent, C., Andras, P., et al., 2016. Compaction of diagenetically altered mudstones Part 1: mechanical and chemical contributions. Mar. Petrol. Geol. 77, 703—713. https://doi.org/10.1016/j.marpetgeo.2016.07.015.
- Greenspan, L., 1977. Humidity fixed points of binary saturated aqueous solutions. J. Res. Nat. Bureau Stand. Sect. A Phys. Chem. 81A (1), 89–96. https://doi.org/10.6028/jres.081A.011.
- Gu, X., Mildner, D.F.R., Cole, D.R., et al., 2016. Quantification of organic porosity and water accessibility in marcellus shale using neutron scattering. Energy Fuel. 30 (6), 4438–4449. https://doi.org/10.1021/acs.energyfuels.5b02878.
- Hagymassy, J., Brunauer, S., Mikihail, R.S., 1969. Pore structure analysis by water vapor adsorption. II. Analysis of five silica gels. J. Colloid Interface Sci. 29 (3), 485–491. https://doi.org/10.1016/0021-9797(69)90132-5.
- Hatch, C.D., Wiese, J.S., Crane, C.C., et al., 2012. Water adsorption on clay minerals as a function of relative humidity: application of BET and Freundlich adsorption models. Langmuir 28 (3), 1790–1803. https://doi.org/10.1021/la2042873.
- Hou, C.H., Yu, B.S., Liu, L., et al., 2021. Water uptake behavior and influence factors of Longmaxi shale: implications from water physisorption and imbibition measurements. Energy Fuel. 35 (15), 11958–11975. https://doi.org/10.1021/acs.energyfuels.1c01413.
- Hu, Y.N., Devegowda, D., Sigal, R., 2016. A microscopic characterization of wettability in shale kerogen with varying maturity levels. J. Nat. Gas Sci. Eng. 33, 1078–1086. https://doi.org/10.1016/j.jngse.2016.06.014.
- Hu, Y.N., Devegowda, D., Sigal, R., et al., 2015. The impact of pore size and kerogen maturity on the behavior of water in organic kerogen nanopores in shales. In: Proceedings of the 3rd Unconventional Resources Technology Conference. https://doi.org/10.2118/178710-MS.
- Huang, L.L., Liu, X.J., Xiong, J., et al., 2020. Experimental on the pore structure characteristics of Longmaxi Formation shale in southern Sichuan Basin, China. Pet 7 (2), 135–141. https://doi.org/10.1016/j.petlm.2020.07.006.
- Ji, W.M., Hao, F., Schulz, H.M., et al., 2019. The architecture of organic matter and its pores in highly mature gas shales of the lower Silurian Longmaxi Formation in the upper Yangtze platform, south China. AAPG (Am. Assoc. Pet. Geol.) Bull. 103 (12), 2909–2942. https://doi.org/10.1306/04101917386.
- Jiang, Z.X., Tang, X.L., Li, Z., et al., 2016. The whole-aperture pore structure characteristics and its effect on gas content of the Longmaxi Formation shale in the southeastern Sichuan basin. Earth Sci. Front. 23 (2), 126–134. https://doi.org/10.13745/j.esf.2016.02.013 (in Chinese).
- Jin, Z.H., Firoozabadi, A., 2014. Effect of water on methane and carbon dioxide sorption in clay minerals by Monte Carlo simulations. Fluid Phase Equil. 382, 10–20. https://doi.org/10.1016/j.fluid.2014.07.035.
- Johnston, C.T., 2010. Probing the nanoscale architecture of clay minerals. Clay Miner. 45 (3), 245–279. https://doi.org/10.1180/claymin.2010.045.3.245.
- Kuila, U., McCarty, D.K., Derkowski, A., et al., 2014. Total porosity measurement in gas shales by the water immersion porosimetry (WIP) method. Fuel 117, 1115–1129. https://doi.org/10.1016/j.fuel.2013.09.073.
- Langmuir, I., 1917. The constitution and fundamental properties of solids and liquids. J. Franklin Inst. 183 (1), 102–105. https://doi.org/10.1016/S0016-0032(17) 90938-X.
- Legens, C., Palermo, T., Toulhoat, H., et al., 1998. Carbonate rock wettability changes induced by organic compound adsorption. J. Petrol. Sci. Eng. 20 (3–4), 277–282. https://doi.org/10.1016/S0920-4105(98)00031-X.
- Li, A.F., Han, W.C., Fang, Q., et al., 2020. Experimental investigation of methane adsorption and desorption in water-bearing shale. Capillarity 3 (3), 45–55. https://doi.org/10.46690/capi.2020.03.02.
- Li, J.Z., Dong, D.Z., Chen, G.S., et al., 2009. Prospects and strategic position of shale gas resources in China. Nat. Gas. Ind. 29 (5), 11–16 (in Chinese).
- Li, J.H., Li, B.B., Gao, Z., et al., 2021. Adsorption behavior, including the thermodynamic characteristics of wet shales under different temperatures and pressures.

- Chem. Eng. Sci. 230, 116228. https://doi.org/10.1016/j.ces.2020.116228.
- Li, J., Li, X.F., Wang, X.Z., et al., 2016. Water distribution characteristic and effect on methane adsorption capacity in shale clay. Int. J. Coal Geol. 159, 135–154. https://doi.org/10.1016/j.coal.2016.03.012.
- Li, J., Li, X.F., Wu, K.L., et al., 2017. Thickness and stability of water film confined inside nanoslits and nanocapillaries of shale and clay. Int. J. Coal Geol. 179, 253–268. https://doi.org/10.1016/j.coal.2017.06.008.
- Li, J.C., Zhang, L.H., Chen, Y.L., 2015. Adsorption behavior study of shale gas: models and new combination approach. In: SPE Asia Pacific Unconventional Resources Conference and Exhibition. November, Brisbane, Australia. https://doi.org/ 10.2118/176880-MS.
- Li, P., Zhang, J.C., Rezaee, R., et al., 2021. Effect of adsorbed moisture on the pore size distribution of marine-continental transitional shales: insights from lithofacies differences and clay swelling. Appl. Clay Sci. 201, 105926. https://doi.org/ 10.1016/j.clay.2020.105926.
- Liang, L.X., Xiong, J., Liu, X.J., et al., 2016. An investigation into the thermodynamic characteristics of methane adsorption on different clay minerals. J. Nat. Gas Sci. Eng. 33, 1046–1055. https://doi.org/10.1016/j.jngse.2016.06.024.
- Liu, H.M., Yuan, P., Liu, D., et al., 2018. Pyrolysis behaviors of organic matter (OM) with the same alkyl main chain but different functional groups in the presence of clay minerals. Appl. Clay Sci. 153, 205–216. https://doi.org/10.1016/iclay.2017.12.028
- Liu, X.J., Zeng, W., Liang, L.X., et al., 2016. Experimental study on hydration damage mechanism of shale from the Longmaxi Formation in southern Sichuan Basin, China. Petroleum 2 (1), 54–60. https://doi.org/10.1016/j.petlm.2016.01.002.
- Mahajan, O.P., Walker, P.L., 1971. Water adsorption on coals. Fuel 50 (3), 308–317. https://doi.org/10.1016/j.fuel.2011.01.005.
- Merkel, A., Fink, R., Littke, R., 2016. High pressure methane sorption characteristics of lacustrine shales from the Midland Valley Basin. Scotland. Fuel 182, 361–372. https://doi.org/10.1016/j.fuel.2016.05.118.
- Merkel, A., Fink, R., Littke, R., 2015. The role of pre-adsorbed water on methane sorption capacity of Bossier and Haynesville shales. Int. J. Coal Geol. 147–148, 1–8. https://doi.org/10.1016/j.coal.2015.06.003.
- Nishino, J., 2001. Adsorption of water vapor and carbon dioxide at carboxylic functional groups on the surface of coal. Fuel 80 (5), 757–764. https://doi.org/10.1016/S0016-2361(00)00136-8.
- Ola, P.S., Aidi, A.K., Bankole, O.M., 2018. Clay mineral diagenesis and source rock assessment in the Bornu Basin, Nigeria: implications for thermal maturity and source rock potential. Mar. Petrol. Geol. 89, 653–664. https://doi.org/10.1016/ i.marpetgeo.2017.10.031.
- Passey, Q.R., Bohacs, K., Esch, W.L., et al., 2013. From oil-prone source rock to gasproducing shale reservoir - geologic and petrophysical characterization of unconventional shale gas reservoirs. In: International Oil and Gas Conference and Exhibition in China. https://doi.org/10.2118/131350-MS.
- Ramachandran, C.E., Chempath, S., Broadbelt, L.J., et al., 2006. Water adsorption in hydrophobic nanopores: Monte Carlo simulations of water in silicalite. Microporous Mesoporous Mater. 90 (1–3), 293–298. https://doi.org/10.1016/ i.micromeso.2005.10.021.
- Rexer, T.F.T., Benham, M.J., Aplin, A.C., et al., 2013. Methane adsorption on shale under simulated geological temperature and pressure conditions. Energy Fuel. 27 (6), 3099–3109. https://doi.org/10.1021/ef400381v.
- Shen, W.J., Li, X.Z., Cihan, A., et al., 2019. Experimental and numerical simulation of water adsorption and diffusion in shale gas reservoir rocks. Adv. Geo-Energy Res. 3 (2), 165–174. https://doi.org/10.26804/ager.2019.02.06.
- Shen, W.J., Li, X.Z., Lu, X.B., et al., 2018. Experimental study and isotherm models of water vapor adsorption in shale rocks. J. Nat. Gas Sci. Eng. 52, 484–491. https://doi.org/10.1016/j.jngse.2018.02.002.

- Timmermann, E.O., 2003. Multilayer sorption parameters: BET or GAB values? Colloids Surf. A Physicochem. Eng. Asp. 220 (1), 235–260. https://doi.org/10.1016/S0927-7757(03)00059-1.
- Wang, J., Liu, H.Q., Qian, G.B., et al., 2021. Mechanisms and capacity of high-pressure soaking after hydraulic fracturing in tight/shale oil reservoirs. Petrol. Sci. 18 (3), 546–564. https://doi.org/10.1007/s12182-020-00524-z.
- Wang, L., Yu, Q.C., 2016. The effect of moisture on the methane adsorption capacity of shales: a study case in the eastern Qaidam Basin in China. J. Hydrol. 542, 487–505. https://doi.org/10.1016/i.ihvdrol.2016.09.018.
- Wang, X.M., Liu, L.F., Wang, Y., 2020. Comparison of the pore structures of lower silurian Longmaxi Formation shales with different lithofacies in the southern Sichuan Basin, China. J. Nat. Gas Sci. Eng. 81, 103419. https://doi.org/10.1016/ i.ingse.2020.103419.
- Wang, X., Mou, C.L., Wang, Q.Y., 2015. Diagenesis of black shale in Longmaxi Formation, southern Sichuan Basin and its periphery. Acta Pet. Sin. 36, 1035–1047. https://doi.org/10.7623/syxb201509002.
- Wang, Y., Qiu, N.S., Borjigin, T., et al., 2019. Integrated assessment of thermal maturity of the upper ordovician—lower silurian wufeng—longmaxi shale in Sichuan Basin, China. Mar. Petrol. Geol. 100, 447–465. https://doi.org/10.1016/ i.marnetgeo.2018.10.025.
- Washburn, E.W., 1921. A note on a method of determining the distribution of pore sizes in a porous material. Proc. Natl. Acad. Sci. U.S.A. 7 (4), 115–116. https://doi.org/10.1073/pnas.7.4.115.
- Weaver, C.E., 1989. Clays, Muds and Shales. Elsevier Science Publishing Company INC. New York, pp. 417–449.
- INC, New York, pp. 417–449.
  Yang, R., Jia, A.Q., He, S., et al., 2020a. Water adsorption characteristics of organic-rich wufeng and Longmaxi shales, Sichuan Basin (China). J. Petrol. Sci. Eng. 193, 107387. https://doi.org/10.1016/j.petrol.2020.107387.
- Yang, R., Jia, A.Q., He, S., et al., 2021. Experimental investigation of water vapor adsorption isotherm on gas-producing Longmaxi shale: mathematical modeling and implication for water distribution in shale reservoirs. Chem. Eng. J. 406, 125982. https://doi.org/10.1016/j.cej.2020.125982.
- Yang, R., Jia, A.Q., Hu, Q.H., et al., 2020b. Particle size effect on water vapor sorption measurement of organic shale: one example from dongyuemiao member of lower jurassic ziliujing formation in jiannan area of China. Adv. Geo-Energy Res. 4 (2), 207–218. https://doi.org/10.26804/ager.2020.02.09.
- Zhang, J.C., Jiang, S.L., Tang, X., et al., 2009. Accumulation types and resources characteristics of shale gas in China. Nat. Gas. Ind. 29 (12), 109–114 (in Chinese).
- Zhang, Y., Yang, B., Yang, Z.X., et al., 2019. Ink-bottle effect and pore size distribution of cementitious materials identified by pressurization—depressurization cycling mercury intrusion porosimetry. Materials 12 (9), 1454. https://doi.org/10.3390/ mai/2001454
- Zhang, Y.F., Yu, B.S., Pan, Z.J., et al., 2020. Effect of thermal maturity on shale pore structure: a combined study using extracted organic matter and bulk shale from Sichuan Basin, China. J. Nat. Gas Sci. Eng. 74, 103089. https://doi.org/10.1016/j.jngse.2019.103089.
- Zhu, D.Y., Jiang, Z.X., Jiang, S., et al., 2021. Water-bearing characteristics and their influences on the reservoir capacity in terrestrial shale reservoirs: a case study of the lower Jurassic Ziliujing Formation in the Northeast Sichuan Basin, China. Mar. Petrol. Geol. 123, 104738. https://doi.org/10.1016/j.marpetgeo.2020.104738.
- Zhu, H.J., Ju, Y.W., Huang, C., et al., 2020. Microcosmic gas adsorption mechanism on clay-organic nanocomposites in a marine shale. Energy 197 (11), 117256. https://doi.org/10.1016/j.energy.2020.117256.
- Zou, C.N., Qun, Z., Dong, D.Z., et al., 2017. Geological characteristics, main challenges and future prospect of shale gas. J. Nat. Gas Geosci. 28 (12), 273–288. https:// doi.org/10.1016/j.jnggs.2017.11.002.